Research Article

Ultrasonic Flaw Imaging via Multipath Exploitation

Yimin D. Zhang,[1] Xizhong Shen,[2] Ramazan Demirli,[1] and Moeness G. Amin[1]

[1] *Center for Advanced Communications, Villanova University, Villanova, PA 19085, USA*
[2] *Electrical and Automatic School, Shanghai Institute of Technology, Shanghai 201418, China*

Correspondence should be addressed to Ramazan Demirli, ramazan.demirli@villanova.edu

We consider ultrasonic imaging for the visualization of flaws in a material. Ultrasonic imaging is a powerful nondestructive testing (NDT) tool which assesses material conditions via the detection, localization, and classification of flaws inside a structure. We utilize reflections of ultrasonic signals which occur when encountering different media and interior boundaries. These reflections can be cast as direct paths to the target corresponding to the virtual sensors appearing on the top and bottom side of the target. Some of these virtual sensors constitute a virtual aperture, whereas in others, the aperture changes with the transmitter position. Exploitations of multipath extended virtual array apertures provide enhanced imaging capability beyond the limitation of traditional multisensor approaches. The waveforms observed at the physical as well as the virtual sensors yield additional measurements corresponding to different aspect angles, thus allowing proper multiview imaging of flaws. We derive the wideband point spread functions for dominant multipaths and show that fusion of physical and virtual sensor data improves the flaw perimeter detection and localization performance. The effectiveness of the proposed multipath exploitation approach is demonstrated using real data.

1. Introduction

Ultrasonic nondestructive evaluation (NDE) has traditionally used single-element sensors for material testing. Most flaw detectors utilize A-scan measurements obtained with monolithic transducers externally placed at different positions on or close to the surface of the material. The synthesized ultrasound array aperture, generated through scanning, provides a series of A-scan data whose intensity profile is used to generate a B-scan cross-section image. Two-dimensional (2D) sensor scanning (e.g., raster scan) over the material generates a collection of B-scan images to obtain a C-scan volume image. These 1D and 2D scanning processes require dedicated hardware to control precise sensor positioning and synchronized data collection. This scanning and imaging process has been typically conducted in laboratory conditions or in industrial material testing facilities using immersion testing techniques. We note, however, that this imaging process is not practical for field testing conditions.

Sensor arrays are more practical for field testing due to their increased coverage area, rapid data collection, and direct imaging capability. Although sensor arrays and beamforming techniques have been used in medical ultrasound for decades [1], their use in ultrasonic NDE has not begun until early 2000s [2]. Recent advances in transducer array manufacturing technology have permitted the use of sensor arrays in ultrasonic NDE, and have enabled significant improvements in the detection, localization, and classification of flaws inside a structure. These advances find wide applications in civil engineering and aerospace, automotive, and other transportation sectors [3, 4]. For example, a total focusing technique utilizes all the transmit and receive data in a 2D array to generate an image of material under consideration [5]. More recently multimode total focusing method is used to combine various wave propagation modes in imaging [6]. With the increased computational power and memory, it is expected that a large amount of data obtained with sensor arrays can be processed in a relatively short and acceptable time. Furthermore, offline processing of large volume data is tolerated in ultrasonic NDE due to the fact that the material structures generally do not change over the course of testing.

The existence of a flaw inside a limited size alloy gives rise to ghosts, which are false targets that appear due to the interreflections of the transmitted signals from the alloy boundaries and the target. Due to the prolonged distance travelled by these multipaths, the ghosts typically position outside the alloy boundaries. However, the ghosts that are located inside the alloy, if not properly identified, can cause clutter and false positives which could make visualization difficult, especially in the presence of multiple flaws. The ghosts may not only appear at positions different from the target location, but also present themselves with different image characteristics. This is attributed to the fact that reflections of ultrasonic signals which occur when encountering different media and interior discontinuities can be cast as direct paths to the target corresponding to the virtual sensors appearing on the top and bottom sides of the target. Some of these virtual sensors constitute a virtual aperture, whereas for others, the aperture changes with the transmitter position. The waveforms observed at the physical as well as the virtual sensors yield additional measurements corresponding to different aspect angles, thus allowing proper multi-view imaging of flaws. Each view has a different point spread function (PSF) and defocuses the target image depending on the location and angle of the respective virtual sensors.

In this paper, we consider multipath exploitations for ultrasonic imaging for the visualization of flaws in a material. In particular, our focus is the knowledge-based approach in which the alloy boundaries are assumed known and the adopted propagation model accurately represents the propagation and scattering phenomena inside the material. While multipath has traditionally been considered as troublesome in radar and wireless communications, significant efforts have been recently made to take advantage of multipath propagation. In wireless communications, diversity gains are obtained by various schemes, including multiple-input multiple-output (MIMO) and opportunistic communications (e.g., [7, 8]). In radar systems, the concept of multipath exploitation radar (MER) is being developed to increase persistent coverage over a large urban terrain. This is achieved by extending the tracking capabilities of existing radar sensor architectures beyond line-of-sight (LOS) using both multipath energy and knowledge of the urban scattering surfaces [9]. Some important results have been reported for urban non-LOS applications, indoor imaging, and other radar applications [10–12]. Multipath exploitation is also reported in acoustic focusing [13] and ultrasonic imaging [6]. Time reversal processing technique is also applied for target detection in a multipath propagation environment [14].

In the underlying ultrasound imaging applications, multipaths, when properly utilized, lead to (1) enlarging the array aperture for image enhancement using both physical and virtual sensors, (2) extension of angle of view of the narrow beamwidth of the ultrasound transducers, allowing improved visibility and array design flexibility, (3) multi-view observations of the flaw leading to better representations and characteristics of flaw volume and perimeter. It is noted that ultrasonic signals experience difficulty in penetrating a flaw, thus the aspect angle of the observation is limited unless access to other sides is available.

In this paper, multipath effects are examined using an aluminum alloy with artificial flaws. Different multipath realizations are considered and their virtual array geometries are identified. For each array geometry, the corresponding point spread function is developed and examined. In essence, exploitation of multipath information in ultrasonic imaging amounts to utilizing the different characteristics of the PSFs and fusing their collective viewing angles of the same target. We show that fusion of physical sensor data and virtual sensor data, due to multipaths, significantly improves flaw detection and characterization. The effectiveness of the proposed multipath exploitation approach is demonstrated through experimental examples.

The rest of the paper is organized as follows. Next section presents multipath propagation in materials with known cubic geometry. Section 3 describes ultrasonic imaging with multipath signals. Section 4 presents point spread function analyses of multipath signals. Section 5 discusses the multipath identification and association method. Section 6 presents experimental examples of multipath imaging. Section 7 concludes the paper.

2. Multipath Propagation Phenomenon

Ultrasound plane waves are subject to reflection and transmission from the boundaries of materials [15]. The propagation model for a beam of plane waves incident normally at a flat boundary is well known; part of the energy is transmitted to the support medium whereas the other part reflects back depending on the impedances of the medium and material. Normally incident propagation creates strong multipath (reverberation) in layered media. This propagation model has been extensively studied and exploited for nondestructive evaluation of layered materials (see e.g., [16]). The propagation model for a beam of plane waves obliquely incident to the medium boundary obeys the Snell's law. Assuming the impedance of the support layer (such as air) is much higher than the material, the majority of the incident energy reflects as longitudinal waves with the reflection angle equal to the incident angle, while a smaller portion of its energy is converted to shear waves. Shear waves reflect with a smaller angle and a lower speed than those of the reflected plane waves. In this paper, we consider longitudinal waves with specular reflections where the incident and reflected waves are coplanar with equal incident and reflected angles. As such, ray tracing models are utilized to predict the multipath signals.

While ultrasound wave reflections from material boundaries are explained with the Snell's law, the ultrasound scattering from material defects is more complex depending on the geometry and size of the object. An object whose size is comparable to the wavelength of the incident ultrasound wave is considered as a point reflector. Objects whose sizes are larger than the wavelength yield specular reflections. However, if the large object has sharp discontinuities or corners, wave diffraction phenomenon occurs at its extremities [15]. For example, an analytical diffraction model is
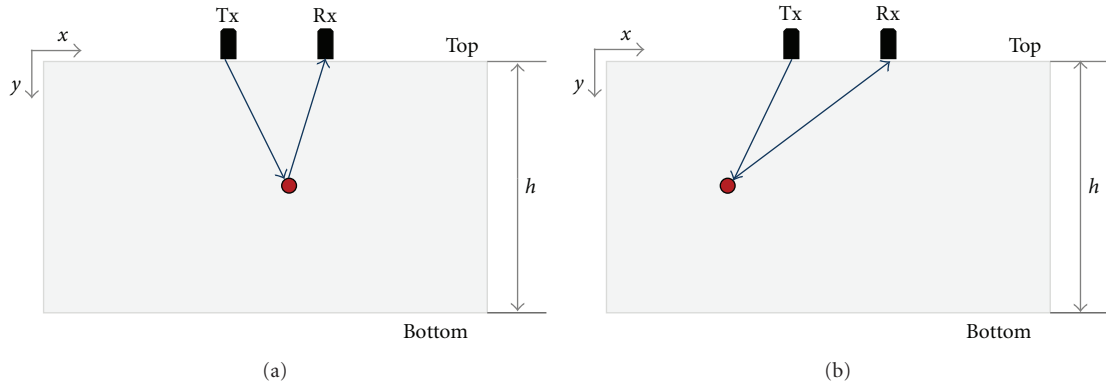
FIGURE 1: Direct paths when the target is between the transmit/receive pair (a) and outside of the pair (b).
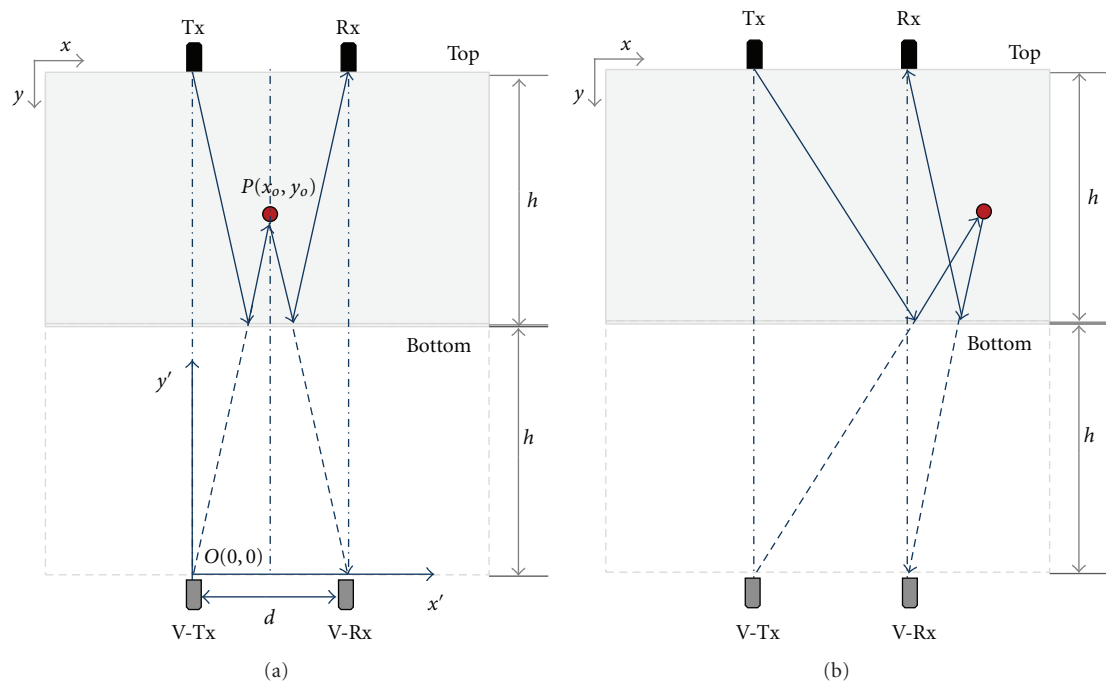

FIGURE 2: Multipath I when the target is between the transmit/receive pair (a) and outside of the pair (b).

developed for a penny-shaped crack in solids and verified experimentally by embedding a large penny-size crack in titanium [17]. In fact, there is a line of time-of-flight diffraction (TOFD) techniques used for flaw sizing based on estimating the time-difference-of-arrival of diffracted echoes from object boundaries [15]. Diffraction echoes are measured in a pitch-catch mode by positioning a pair of angle probes (transmitting and receiving transducers) far enough on the material's surface to see the extent of the crack. As such, measurements of diffraction echoes require angled and wide-beam ultrasound radiation and adjustment of the position of probes during acquisition. In this paper, we utilize direct and multipath specular reflections that can be observed with a fixed ultrasonic transducer array. These reflections are due to the plane waves which travel with a known uniform speed in materials.

We focus on multipaths due to bottom and top surface of alloys. In assuming wide alloys or limited transducer beamwidth, reflections from the sides of the alloy can be ignored. Thus, among a number of possible multipath patterns [15], we consider dominant two-way propagation patterns as illustrated in Figures 1, 2, and 3 where the black solid lines denote real paths and dashed lines imply virtual (image) paths. Figures 1(a) and 1(b) show the direct paths for two possible cases of the flaw. For the first case (a), the flaw lies inside the vertical strip defined by the transmit/receive transducer pair, whereas in the second case (b), the flaw is outside the strip. In Figure 2(a), reflections occurring at the bottom surface yield a W-shape propagation path. It can be equivalently represented by using the Λ-shape virtual path, with corresponding virtual transmit and receive transducers located at the bottom of the mirrored object. As such, in addition to the top view of the flaw accessed from the direct path, the exploitation of the multipath, in this scenario, will provide a bottom view of the flaw. On the other hand,
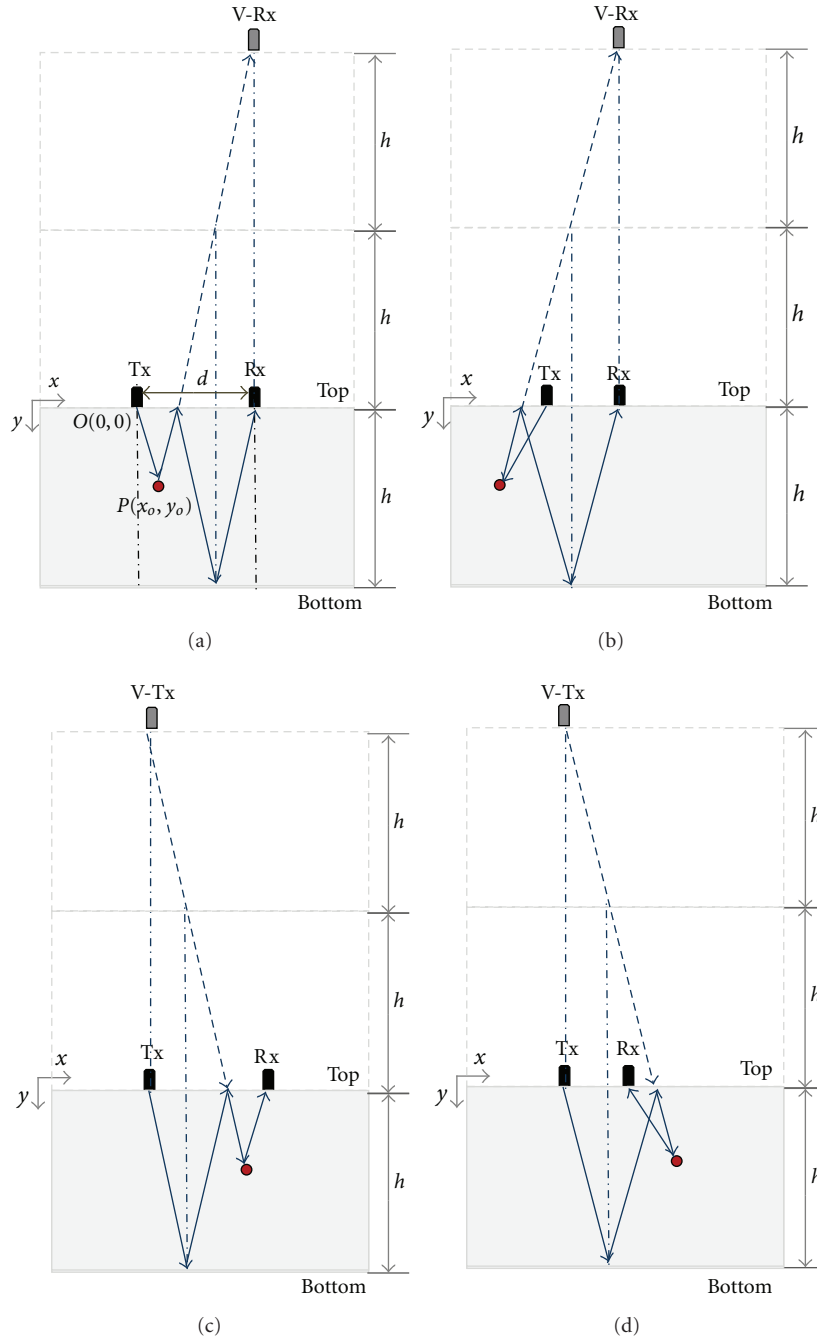
FIGURE 3: Multipath II-A with the virtual receiver when the target is between the transmit/receive pair (a) and outside of the pair (b). Multipath II-B with virtual transmitter when the target is between the transmit/receive pair (c) and outside of the pair (d).

the multipath II-A pattern depicted in Figures 3(a) and 3(b) include reflections from the top and bottom surfaces of a one-way path (shown in Figure 3(a) for the path from the flaw to the receive transducer) which results in a virtual position of the receive transducer with a different top view of the flaw. Multipath II-B pattern, depicted in Figures 3(c) and 3(d), includes top and bottom reflections only between transmit transducer and the flaw (not from the flaw to the receive transducer), which results in a virtual position of the transmit transducer with a different top view aspect of the flaw.

The ranges for various multipath signals can be predicted based on the known depth of the alloy (h) and transmit/receive sensor coordinates. We show in the Appendix that multipath I and II-A signals (those depicted in Figure 2(a) and Figure 3(a)) approximately lie in range $[2h \ 4h]$, when h is much larger than the distance between the T/R sensor pair, d. Multipath I and II signals coincide when the target is exactly at the center of the alloy inside the T/R pair strip, that is, when the target is at the coordinates $x = d/2$, $y = h/2$. For all other cases, multipath I and multipath II signals will be separable.

3. Signal Model and Ultrasonic Imaging

3.1. Signal Model. We consider an ultrasonic imaging system, where a single transducer transmits a wideband waveform, and several other transducers receive echoes from the tested material. This process is repeated for all transducers in the system. By the virtue of sequential waveform transmission and nonoverlapping nature of the transmitted signals, the transmitted signals can be separated at the receivers. As such, a multiple-input multiple-output (MIMO) system is implemented which allows a virtual aperture to by synthesized [18]. The MIMO system configuration outperforms traditional array configurations in target resolution and detection, especially, when the signal-to-noise ratio (SNR) is high. In this paper, we do not address the MIMO aspect of the imaging system, as it is implicit in our approach. Rather, we focus on another form of virtual sensors generated by the multipaths. The latter allows different aspect angles to the target, allowing detection of the target boundaries and perimeters.

Denote the signal emitted from the transmit transducer as $s_T(t)$. Let N be the total number of transducers. The signal received at the nth receive transducer corresponding to the mth transmit transducer position is denoted as $r_{mn}(t)$, where $m = 1, \ldots, N$ and $n = 1, \ldots, N$ with $m \neq n$. The received signal $r_{mn}(t)$ is considered as the convolution of the transmitted signal, $s_T(t)$, and the respective propagation channel associated with the mth transmit transducer and the nth receive transducer, $h_{mn}(t)$. That is,

$$r_{mn}(t) = h_{mn}(t) * s_T(t), \tag{1}$$

where $*$ denotes the convolution operation.

3.2. Ultrasonic Imaging Based on Direct Reflection Path. We assume that the respective positions of the transmit-and-receive array elements are assumed to be known in a three-dimensional Cartesian space, that is, the mth transmit transducer is located at $T_m = (x_{Tm}, y_{Tm}, z_{Tm})$, and the nth receive transducer is located at $R_n = (x_{Rn}, y_{Rn}, z_{Rn})$. The coordinate system is shown in Figure 4. Consider a region of interest (ROI) which is a two-dimensional cross-section under the linear array and corresponds to the plane as shown in Figure 4. We utilize a receive mode backprojection beamforming algorithm to construct internal images of materials [19]. The imaging can be performed in coherent or noncoherent sense [20]. Coherent imaging takes the amplitude and phase information into consideration when adding the signals received at each sensor, whereas only the amplitude information is incorporated in noncoherent imaging. The signal that is reflected from a hypothetical target located at the position $P(x_P, y_P, z_P)$ is then received with different delays at each receiver. The signal corresponding to the direct reflection path recorded at the nth receive transducer is given by

$$r_{mn}^{[d]}(t) = a_{mn}^{[d]}(P) s_T \left(t - \tau_{mn}^{[d]}(P) \right), \tag{2}$$

where $a_{mn}^{[d]}(P)$ is the reflectivity of the flaw that also accounts for the propagation loss, and $\tau_{mn}^{[d]}(P)$ denotes the delay for
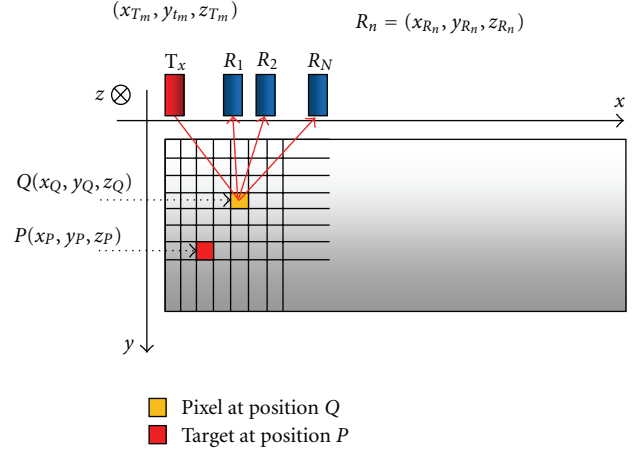

FIGURE 4: Transducer array and imaging geometry.

the signal to travel from the mth transmit transducer T_m to the target at P and then from location P to the nth receive transducer R_n. The superscript $^{[d]}$ is used to emphasize the direct reflection path. Assuming a homogeneous material with ultrasonic propagation speed of v in the material (the variation of the speed in the material and its compensation is considered in [18]), the time delay corresponding to any pixel Q in the image, located at (x_Q, y_Q, z_Q), can be calculated as

$$\tau_{mn}^{[d]}(Q) = \frac{\left\| \left(x_{Tm}, y_{Tm}, z_{Tm} \right) - \left(x_Q, y_Q, z_Q \right) \right\|}{v} + \frac{\left\| \left(x_{Rn}, y_{Rn}, z_{Rn} \right) - \left(x_Q, y_Q, z_Q \right) \right\|}{v}, \tag{3}$$

where $\| \cdot \|$ denotes the Euclidean norm operation. This imaging principle is illustrated in Figure 4.

The image intensity $I(Q)$ of every pixel Q in the image is obtained by adding the weighted time-delayed $N(N-1)$ received signals and correlating the resulting signal with the transmitted signal. The weights influence the point spread function (PSF) and can be chosen to control the PSF main lobe and side lobe characteristics [18]. Therefore, the intensity at pixel Q, using coherent imaging technique, can be written as

$$
\begin{aligned}
I(Q) &= \left. \sum_{m=1}^{N} \sum_{\substack{n=1 \\ n \neq m}}^{N} w_{mn}^{[d]}(Q) r_{mn} \left(t + \tau_{mn}^{[d]}(Q) \right) * s_T(t) \right|_{t=0} \\
&= \sum_{m=1}^{N} \sum_{\substack{n=1 \\ n \neq m}}^{N} w_{mn}^{[d]}(Q) a_{mn}^{[d]}(P) s_T \left\{ t + \tau_{mn}^{[d]}(Q) - \tau_{mn}^{[d]}(P) \right\} \\
&\quad \left. * s_T(t) \right|_{t=0},
\end{aligned} \tag{4}
$$

where $w_{mn}^{[d]}(Q)$ is the weight corresponding to the mth transmit transducer and the nth receiver transducer. The

cross-correlation performs matched filtering and improves the output signal-to-noise ratio (SNR).

3.3. Ultrasonic Imaging Based on Multipath Signals. Similar to the direct reflection, we now consider three types of multipaths that are associated with the target located at $P = (x_P, y_P, z_P)$. The signal at the receive transducer R_n corresponding to the mth transmit transducer is given by

$$r_{mn}^{[i]}(t) = a_{mn}^{[i]}(P)s_T\left(t - \tau_{mn}^{[i]}(P)\right), \quad (5)$$

where the superscript $[i]$ with $i = 1, 2, 3$ denotes the index of multipath I, multipath II-A, and multipath II-B, respectively.

Denoting h as the height of the metallic object, the time delays corresponding to a point target P, located at (x_P, y_P, z_P), can be, respectively, calculated for the direct and multipaths as follows.

Direct reflection path

$$\tau_{mn}^{[d]}(P) = \frac{\left\|\left(x_{Tm}, y_{Tm}, z_{Tm}\right) - (x_P, y_P, z_P)\right\|}{v} \\ + \frac{\left\|(x_{Rn}, y_{Rn}, z_{Rn}) - (x_P, y_P, z_P)\right\|}{v}. \quad (6a)$$

Multipath I

$$\tau_{mn}^{[1]}(P) = \frac{\left\|\left(x_{Tm}, 2h - y_{Tm}, z_{Tm}\right) - (x_P, y_P, z_P)\right\|}{v} \\ + \frac{\left\|(x_{Rn}, 2h - y_{Rn}, z_{Rn}) - (x_P, y_P, z_P)\right\|}{v}. \quad (6b)$$

Multipath II-A

$$\tau_{mn}^{[2]}(P) = \frac{\left\|\left(x_{Tm}, y_{Tm}, z_{Tm}\right) - (x_P, y_P, z_P)\right\|}{v} \\ + \frac{\left\|(x_{Rn}, y_{Rn} - 2h, z_{Rn}) - (x_P, y_P, z_P)\right\|}{v}. \quad (6c)$$

Multipath II-B

$$\tau_{mn}^{[3]}(P) = \frac{\left\|\left(x_{Tm}, y_{Tm} - 2h, z_{Tm}\right) - (x_P, y_P, z_P)\right\|}{v} \\ + \frac{\left\|(x_{Rn}, y_{Rn}, z_{Rn}) - (x_P, y_P, z_P)\right\|}{v}. \quad (6d)$$

Note that these multipaths, when processed using the actual transducer positions, will result in images outside the ROI. For multipath exploitations, however, we will synthesize their respective images using the virtual transducer positions, respectively, located at $T_m^{[1]} = (x_{Tm}, 2h - y_{Tm}, z_{Tm})$, $R_n^{[1]} = (x_{Rn}, 2h - y_{Rn}, z_{Rn})$ for multipath I, $T_m^{[2]} = T_m = (x_{Tm}, y_{Tm}, z_{Tm})$, $R_n^{[2]} = (x_{Rn}, y_{Rn} - 2h, z_{Rn})$ for multipath II-A, and $T_m^{[3]} = (x_{Tm}, 2h - y_{Tm}, z_{Tm})$, $R_n^{[3]} = R_n = (x_{Rn}, y_{Rn}, z_{Rn})$ for multipath II-B. In this way, multipath images will align and display the true position and size of the flaw. Specifically, multipath I image visualizes the bottom view of the flaw, whereas the other two images visualize the flaw from the top view.

4. Point Spread Functions

The virtual sensors reveal different segments of the flaw by the virtue of being placed at distinct positions from their physical sensors counterparts. Additionally, the new positions of the virtual sensors could be closer or farther from the target than the physical array sensors. As such, different segments of the flaw may be imaged with different resolutions. To demonstrate this fact, we drive in this section the point spread functions (PSFs) associated with the direct path, multipath I, and multipath II for a MIMO array configuration comprised of N ultrasonic transducers. The PSF is the response of the array imaging system to a point target. It captures the imaging characteristics of an array hence will be used herein for assessing the imaging performance associated with the direct path and multipaths. The PSF at an imaging point Q is derived in the frequency domain [19] considering an ideal point target located at P

$$I(Q) = \sum_{m=1}^{N} \sum_{\substack{n=1 \\ n \neq m}}^{N} w_{mn} \int_{\Omega} R_{mn}(f) S^*(f) e^{j2\pi f \hat{\tau}_{mn}(Q)} df, \quad (7)$$

where $R_{mn}(f)$ is the Fourier transform of the signal received by the nth receiver due to the mth transmitter, $S(f)$ is the Fourier transform of the transmitted waveform, w_{mn} is a weighting applied to the signal received by the nth receiver due to the mth transmitter, Ω is the bandwidth of the waveform, and $\hat{\tau}_{mn}(Q)$ is the estimated total propagation delay of the signal in traveling from the mth transmit element to the imaging point Q, and then back to the nth receive element. If we assume no dispersion, no attenuation, and monochromatic waveforms, the received signal can be written as

$$R_{mn}(f) = S(f)e^{-j2\pi f \tau_{mn}(P)}, \quad (8)$$

where $\tau_{mn}(P)$ represents the delay due to the target at P when a pulse is emitted from the mth transducer and the back-scattered signal is received from the nth transducer. We assume an ideal pulse with bandwidth B, that is, $|S(f)| = 1$, for $f_o < f < f_o + B$. Such a pulse can be closely emulated with a windowed Chirp function. The pulse bandwidth is sampled with frequencies as $f_k = f_0 + k\Delta f$ for $k = 0, \ldots, N_f - 1$, where N_f is the number of frequencies and $\Delta f = B/N_f$. Inserting (8) into (7) and sampling the bandwidth with the available discrete frequencies, the pixel value at imaging point Q (i.e., the PSF) can be written as follows:

$$I(Q) = \sum_{m=1}^{N} \sum_{\substack{n=1 \\ n \neq m}}^{N} w_{mn} \sum_{k=1}^{N_f - 1} e^{j2\pi(f_0 + k\Delta f)(\hat{\tau}_{mn}(Q) - \tau_{mn}(P))}. \quad (9)$$

It can be observed that the PSF highly depends on the target location P, the transducer array geometry and its characteristics, and the number of frequencies used in synthesizing the pulse. As such, these factors determine beamforming image quality. It is important to note that, given the wavelength, flaw range, and array extent, it is clear that we deal, in this paper, with a near-field problem. As
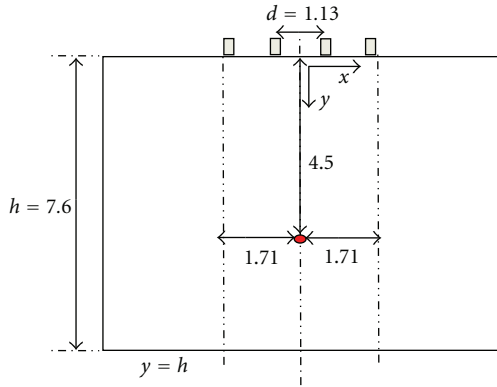
FIGURE 5: Simulated imaging configuration used for PSF computations (units are in cm).

such, the image cannot be simply cast as a convolution of the PSF and spatial extent of the flaw. However, the PSF in the underlying problem remains indicative to image quality and can reveal the expected defocusing or blurring of the target associated with different multipaths.

In order to assess multipath imaging performance, we derive the PSFs due to multipath I and II and compare these to that of the direct path for near-field ultrasound flaw imaging. A simulated sensor array configuration for imaging a point target in a metallic alloy is illustrated in Figure 5. This simulation is intended to emulate experimental imaging conditions in our lab. A point target is assumed to be at the location $(0, 4.5)$ cm in the near-field of a 4-element linear transducer array where the center point of the array denotes the origin $(0, 0)$. The transducers are spaced with 1.13 cm (4λ) where $\lambda = 2.82$ mm is the wavelength of the propagating sound. The aperture of the transducer array is 12λ. A wideband chirp signal of length 50 ms with a 2.25 MHz center frequency and 2 MHz bandwidth is used to emulate an ideal pulse transmission.

First, we compute the PSF for the direct path based on the array geometry shown in Figure 5 and wideband chirp excitation. The intensity of the image point Q (9) is computed along the cross-range of the target and within the array aperture $[-6\lambda \ 6\lambda]$. This PSF is shown in Figure 6 in a solid black line. For computing the PSF of multipath I and II, we utilize virtual transmitter and receivers due to these multipaths as shown in Figures 2 and 3. The delays corresponding to the targets ($\tau_{mn}(P)$) and the test point Q ($\hat{\tau}_{mn}(Q)$) for multipaths are computed based on these virtual transmitter and receiver locations. These delays are used in PSF computations (see (9)) for a set of test points along the cross-range of the target. The virtual array for multipath I is a mirror image of the physical array with respect to the $y = h$ axis (i.e., the bottom surface of the material) and is placed at $y = 2h$ axis. As such, Multipath I virtual array views the target from a larger distance than that is seen from the physical array. This causes the main lobe of the PSF to be widened compared to that of the direct path PSF, whereas the side-lobes are reduced. For computing multipath II PSF, we utilize virtual transmitters or receivers positioned at $y = -2h$ line. More specifically, for multipath
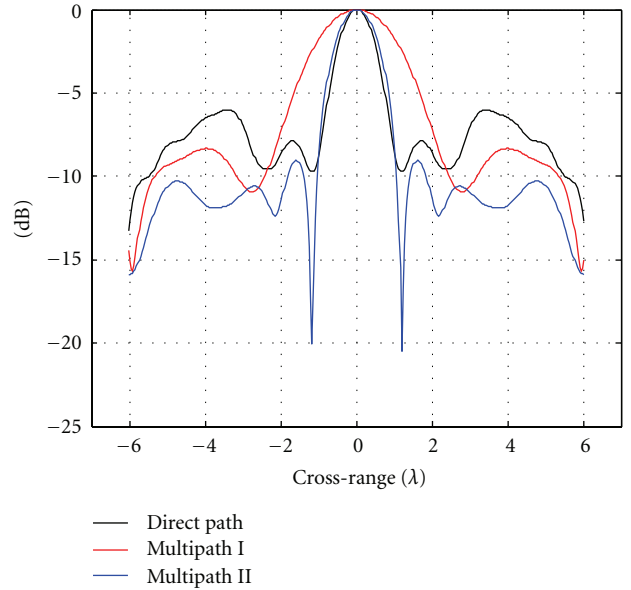

FIGURE 6: Cross-range PSFs for direct path (black line), Multipath I (red line) and Multipath II (blue line) based on wideband chirp excitation for the point target with the imaging array in near field as shown in Figure 5.

II-A, the virtual receivers are positioned at $y = -2h$ line, while the transmitter stays at its original location. Similarly, for multipath II-B, the virtual transmitter is positioned at $y = -2h$ line, while the receivers stay at their original locations, as shown in Figure 3. The PSFs associated with these two multipaths are combined into one PSF, since these two multipaths are generally unresolvable. This PSF is shown in Figure 6 in solid blue line. While the main-lobe of the Multipath II PSF is almost identical to that of the direct path, the side-lobes are reduced markedly, hence offering an improved imaging performance.

5. Multipath Identification and Association

When the image of the direct reflection path is synthesized and the location of a potential flaw, P, is identified, it is possible to identify the region where the images associated with the multipaths are likely to be located. When the flaw is assumed to be a point target, the respective delays corresponding to different paths can be computed from (6b)–(6d). Note that the actual time delay may be affected by the flaw shape and size, inhomogeneous propagation characteristics, and even the surface couplings in the transducers. Therefore, the objective of multipath association is to identify the likely multipath signals in the received waveforms and then process these signals to synthesize the multipath images.

To help identifying the direct reflection and multipath signals, we consider the received signal waveforms in terms of different phases. The first and the second phases are separated by the time delay corresponding to the bottom reflection. For specular bottom reflection, the reflection point corresponding to the mth transmit

transducer $T(x_{Tm}, y_{Tm}, z_{Tm})$ and the nth receive transducer $R_n(x_{Rn}, y_{Rn}, z_{Rn})$ is located at $((x_{Tm} + x_{Rn})/2, h, (z_{Tm} + z_{Rn})/2)$. Ignoring the gap between the transducers and the top surface (i.e., $y_{Tm} = y_{Rn} = 0$), the kth and the $(k+1)$th phases are separated by the time delay $(1/v)[((x_{Tm} - x_{Rn})/2)^2 + (2kh)^2 + ((z_{Tm} - z_{Rn})/2)^2]^{1/2}$. In this way, the waveform corresponding to the direct reflection path is located in Phase I, whereas the first-order multipath waveforms illustrated in Figures 2 and 3 are located in Phase II.

Phases I and II are used in the backprojection imaging to align the target images corresponding to the different multipaths. Any signal returns received over Phase I will be attributed to the physical array, whereas the returns of delays longer than the two-way propagation time to the bottom of the alloy will be attributed to cases involving virtual sensors. It is important to note that, according to the multipath configurations depicted in Figure 3, there is always a combination of physical and virtual sensors when considering multipath II. Although multipath I and multipath II both lie in Phase II, one can separate them according to their respective time delays. It can be observed that the direct-path delay and multipath I delay are approximately equally positioned on both sides away from the delay corresponding to the alloy bottom, which is very evident in Figure 2. One can, therefore, apply a time window to isolate multipaths I and II, provided that they are separable, as it is the case in the underlying example.

6. Experimental Examples

6.1. Experiment Settings.

This section provides the results of our experimental studies. An aluminum block (alloy number 6061) of dimensions 12 in $\times$ 6 in $\times$ 3 in (304.8 mm $\times$ 152.4 mm $\times$ 76.2 mm) is used as the test specimen. Figure 7 shows a horizontal hole with a diameter of 9.24 mm going through the block, which simulates a specular flaw.

The waveform generation and observation are performed using Acousto/Ultrasonics system manufactured by Physical Acoustics. A train of 3 ms chirp waveform pulses with a frequency range between 1 MHz and 4 MHz were generated using an ARB-1410 arbitrary waveform generating board equipped in system, and the return signals were recorded by two PCI-2 two-channel AE data acquisition cards equipped in the same system with a sampling rate of 40 MHz [21]. A 20/40/60 dB preamplifier from Physical Acoustics is inserted between each receive transducer and the respective receiver PCI board. Olympus V133-RM contact transducers with a 2.25 MHz center frequency are used as both transmitter and receivers [22]. Four uniform linear transducer positions separated by an interelement spacing of 11.43 mm are considered. When a transducer at one position is used for transmission, transducers at the other three positions are used for receiving. By sequentially changing the transducer functions, a combination of 12 observations are recoded to synthesize an MIMO system.

Because chirp waveforms are transmitted, the received signal is first compressed using matched filtering [23]. Then,
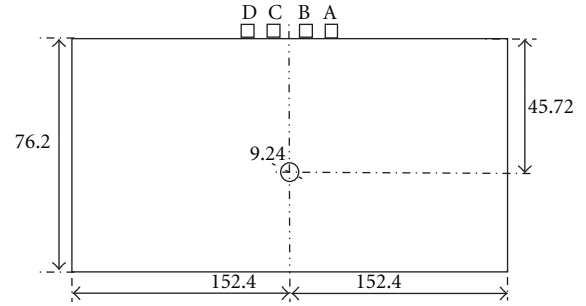

FIGURE 7: Dimensions of the aluminum alloy (unit: mm).

the Hilbert transform is applied to the received signals to form their analytical signal expressions for multipath identification and imaging.

6.2. Results.

The transducers are positioned on the top surface of the aluminum alloy ($y = 0$), and their x positions relative to the flaw center are, respectively, 17.145 mm (position A), 5.715 mm (position B), -5.715 mm (position C), and -17.145 mm (position D).

Table 1 summarizes the predicted and measured time delays of the direct and multipath signals from the flaw for all possible combinations of transmission and reception using the four transducers. The time delays are recorded for the flaw echo, echo from the bottom surface of the alloy, and multipath I and II echoes. The predicted time delays are calculated by tracing the direct and multipaths based on the geometry of the hole and transducer array as shown in Figure 7. The direct reflection echo from the flaw appears around 13.5 μs, whereas the multipath I echo appears around 32.3 μs. Multipath II-A and II-B echoes are both located around 37 μs and are generally unresolvable. As it is seen from the table, the measured time delays are in good agreement with the predicted time delays, indicating the validity of the multipath models.

Figure 8 shows the received waveform envelopes after matched filtering for all possible combinations of transmit/receive transducer pairs. It is evident that all waveform envelopes show clear direct reflection path (approximately between 13.0 and 14.0 μs) and bottom reflection (approximately between 24.1 and 24.6 μs), whereas the level of multipath signals depends on the transducer positions, because some multipaths corresponding to certain transducer positions may be obstructed by the hole itself. In general, the combination of using transducers positions A and D yields a higher multipath signal level.

Figure 9 shows the imaging results generated using different multipaths with the correct location and size of the flaw marked with a white circle. Figure 9(a) shows the image generated using the direct reflection path. The top of the hole is clearly identified. Multipath I yields an image showing the bottom of the hole, as depicted in Figure 9(b). Figure 9(c) shows the results obtained from multipath scenarios II. Since these images represent reflections at different sensor positions, image fusion can be applied. Figure 9(d) shows the fused image obtained by a simple sum of the previous three
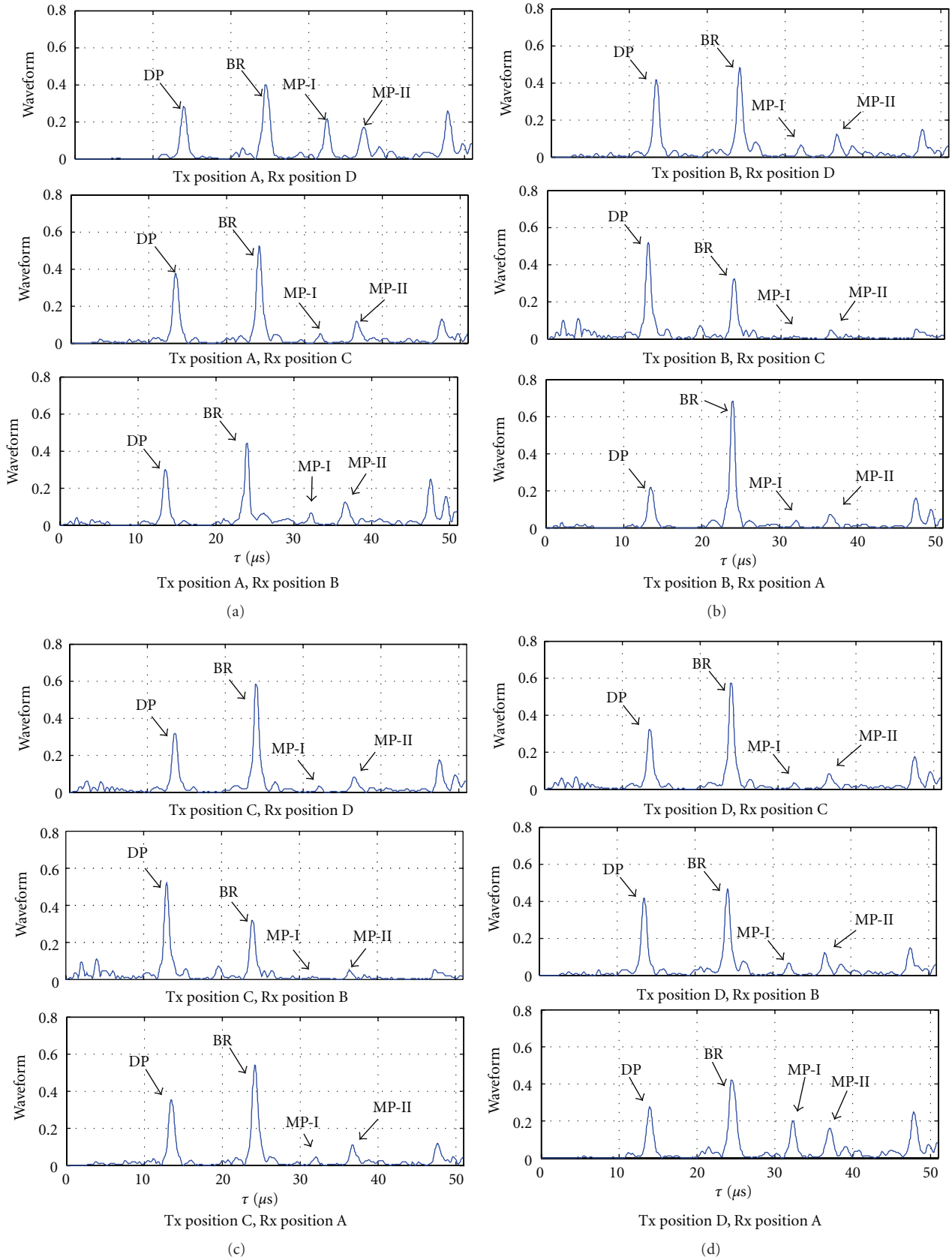
FIGURE 8: (a) Received waveform envelopes at sensors B, C, and D corresponding to transmitter A. (b) Received waveform envelopes at sensors A, C, and D corresponding to transmitter B. (c) Received waveform envelopes at sensors A, B, and D corresponding to transmitter C. (d) Received waveform envelopes at sensors A, B, and C corresponding to transmitter D.

TABLE 1: Predicted and measured time delays of multipath signals for the specular flaw shown in Figure 7 (unit: μs).

Transmit position	Receive position	Calculated time delay					Measured time delay			
		Bottom	Flaw	MP I	MP II-A	MP II-B	Bottom	Flaw	MP I	MP II-A/B
A	D	24.592	13.986	32.562	37.569	37.569	24.600	14.050	32.450	37.200
	C	24.265	13.513	32.364	37.465	37.096	24.280	13.550	32.180	36.880
	B	24.067	13.513	32.364	37.465	37.096	24.070	13.600	32.330	36.730
B	D	24.265	13.513	32.364	37.096	37.465	24.280	13.570	32.180	36.800
	C	24.067	13.040	32.166	36.991	36.991	24.070	13.030	32.180	36.520
	A	24.067	13.513	32.364	37.096	37.465	24.070	13.550	32.270	36.630
C	D	24.067	13.513	32.364	37.096	37.465	24.070	13.630	32.220	36.700
	B	24.067	13.040	32.166	36.991	36.991	24.070	13.030	32.380	36.500
	A	24.265	13.513	32.364	37.096	37.465	24.280	13.550	32.180	36.850
D	C	24.067	13.513	32.364	37.465	37.096	24.070	13.630	32.220	36.670
	B	24.265	13.513	32.364	37.465	37.096	24.280	13.550	32.180	36.800
	A	24.592	13.986	32.562	37.569	37.569	24.600	14.030	32.430	37.180

(a) Direct path

(b) Multipath I

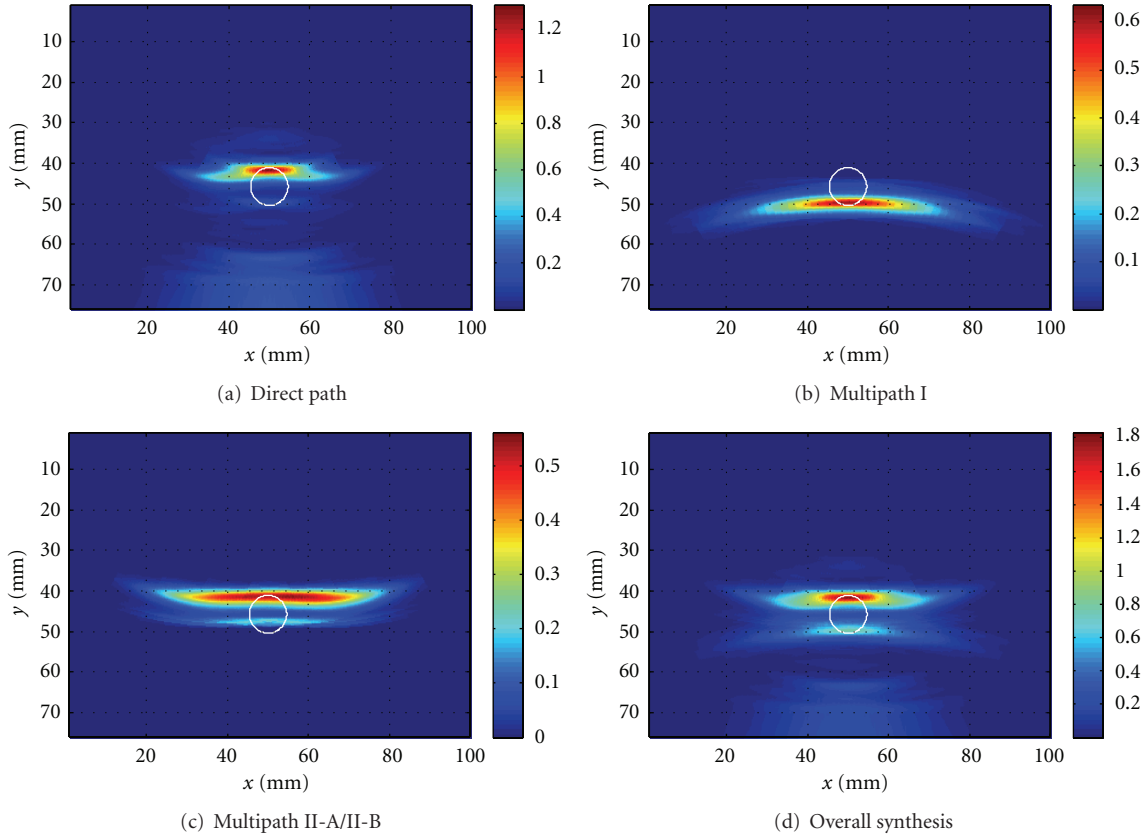(c) Multipath II-A/II-B

(d) Overall synthesis

FIGURE 9: Ultrasound imaging of a hole via multipath exploitation.

images. It is evident that the size of the hole is now revealed from the fusion result, which is otherwise unavailable if only the direct reflection observations were used.

7. Conclusions

Multipath propagation was explored in ultrasonic imaging for the purpose of nondestructive testing. Reflections from the flaw, when combined with reflections from the alloy boundaries, provide an opportunity to reveal segments of the flaw that are shadowed due the limited range penetration of ultrasound waves. Knowledge-based multipath exploitation was made possible by assumed known dimensions of a metallic alloy and resolvable signal arrivals. We focused on three categories of multipaths, all traced to reflections in the vertical plane including the transducers and flaw, and ignoring reflections from the alloy sides. By identifying multipaths that reflect at the known top and bottom surfaces, virtual sensors can be identified. The locations of these sensors permit visualizations of the shadowed regions

which otherwise is difficult to obtain from only the direct reflection signals. With the translation of the virtual sensor in both dimensions, more aspect angles to the target become available, aiding in the determination of the flaw type and perimeter. The point spread functions corresponding to the different multipath types were derived and shown to be different, causing the image quality to vary with multipath. The proposed multipath exploitation is supported by analysis and verified by experimental data.

Appendix

A. Minimum and Maximum Path Lengths for Multipath I and II

We show the minimum and maximum path lengths for multipath I (Figure 2(a)) and multipath II (Figure 3(a)). These minimum and maximum lengths will determine the range of the two-way propagation time delays from the transmitter and back to the receiver. This will, in turn, aid in separating multipaths from the direct path and associate them with their respective virtual arrays.

For multipath I, we fix the origin at the virtual transmitter (V-Tx) location and denote as O $(0, 0)$. Then the flaw location P is assigned as (x_o, y_o) according to the (x', y') axis representation in Figure 2(a). Further, assuming the target is in the strip between the transducer and receiver pair and between the top and bottom surface, the target point P coordinates change in ranges as, $0 < x_o < d$ and $h < y_o < 2h$, where d denotes the distance between the transmitter and receiver, and h denotes the depth of the material. The total path length from virtual transmitter (V-Tx) to the target and from target to the virtual receiver (V-Rx) can be written as follows:

$$L_1(x_0, y_0) = \sqrt{x_0^2 + y_0^2} + \sqrt{(d - x_o)^2 + y_0^2} \qquad (A.1)$$

We find the minimum and maximum values of this path via maxima points. By taking the partial derivative of the above equation with respect to x_o and setting it equal to 0 yields

$$\frac{\partial L_1(x_0, y_0)}{\partial x_0} = \frac{x_o}{\sqrt{x_0^2 + y_0^2}} - \frac{(d - x_o)}{\sqrt{(d - x_o)^2 + y_0^2}} = 0. \qquad (A.2)$$

The maxima point x_o satisfying the above equation can be derived as $\tilde{x}_o = 0.5d$. It can be readily shown that the path length $L_1(x_0, y_0)$ is minimized at this maxima point. Similarly, taking the partial derivative of $L_1(x_0, y_0)$ with respect to y_o and setting it equal to 0 yields

$$\frac{\partial L_1(x_0, y_0)}{\partial y_0} = \frac{y_o}{\sqrt{x_0^2 + y_0^2}} + \frac{y_o}{\sqrt{(d - x_o)^2 + y_0^2}} = 0. \qquad (A.3)$$

From the above equation, the maxima point can be found at $y_o = \tilde{y}_o = 0$. It can be readily shown that this point minimizes $L_1(x_0, y_0)$. Further, it can be seen from (A.1) that $L_1(x_0, y_0)$ is a monotonically increasing function of y_o. Since y_o changes in range, $h < y_o < 2h$, the path length $L_1(x_0, y_0)$ will be minimum at target location $(0.5d, h)$, and will be

maximum at target locations $(0, 2h)$ and $(d, 2h)$. As a result, the minimum path length can be calculated as

$$L_1(0.5d, h) = 2\sqrt{(0.5d)^2 + h^2}. \qquad (A.4)$$

Similarly, the maximum path length can be calculated as

$$L_1(0, 2h) = L_1(d, 2h) = 2h + \sqrt{d^2 + (2h)^2}. \qquad (A.5)$$

Furthermore, assuming the material depth is much larger than the distance between the transmitter and receiver, that is, $h \gg d$, the minimum and maximum path lengths can be approximated as

$$\{L_1\}_{\min} = L_1(0.5d, h) \cong 2h,$$
$$\{L_1\}_{\max} = L_1(0, 2h) = L_1(d, 2h) \cong 4h. \qquad (A.6)$$

Therefore, multipath I will approximately be in range $[2h\ 4h]$ and its arrival time will be confined to the time interval, $[2h/v\ 4h/v]$, where v is the speed of sound in the material.

For multipath II, we first fix the origin at transmitter (Tx) location and denote as O $(0, 0)$ (See Figure 3(a)). Then, the flaw location P is assigned as (x_o, y_o) according to the (x, y) axis representation in Figure 3(a). Further, assuming the target is in the strip between the transducer and receiver pair and between the top and bottom surface, the target point P coordinates change in ranges as, $0 < x_o < d$ and $0 < y_o < h$. Then, the total path length from the transmitter (Tx) to the target and from target to the virtual receiver (V-Rx) can be written as

$$L_2(x_0, y_0) = \sqrt{x_0^2 + y_0^2} + \sqrt{(d - x_o)^2 + (2h + y_0)^2}. \qquad (A.7)$$

By taking the partial derivative of the above equation with respect to x_o and setting it equal to 0 yields

$$\frac{\partial L_2(x_0, y_0)}{\partial x_0} = \frac{x_o}{\sqrt{x_0^2 + y_0^2}} - \frac{(d - x_o)}{\sqrt{(d - x_o)^2 + (2h + y_0)^2}} = 0. \qquad (A.8)$$

The maxima point x_o satisfying the above equation can be derived as $x_m = y_0 d/2(h + y_0)$. It can be readily shown that the path length $L_2(x_0, y_0)$ is minimized at this maxima point. Similarly, taking the partial derivative of $L_2(x_0, y_0)$ with respect to y_o and setting it equal to 0 yields

$$\frac{\partial L_2(x_0, y_0)}{\partial y_0} = \frac{y_o}{\sqrt{x_0^2 + y_0^2}} + \frac{2h + y_o}{\sqrt{(d - x_o)^2 + (2h + y_0)^2}} = 0. \qquad (A.9)$$

From above equation, the maxima point minimizing $L_2(x_0, y_0)$ can be found as $y_o = \tilde{y}_o = 0$. Further, it can be seen from (A.7) that $L_2(x_0, y_0)$ is a monotonically increasing function of y_o. Since y_o changes in range, $0 < y_o < h$, the path length $L_2(x_0, y_0)$ will be minimum at target location $(x_m, 0)$, and maximum at locations $(0, h)$ and (d, h). As a result, the minimum path length can be calculated as

$$L_2(x_m, h) = x_m + 2\sqrt{(d - x_m)^2 + (2h)^2}. \qquad (A.10)$$

Similarly, the maximum path length can be calculated as

$$L_2(0, h) = h + \sqrt{d^2 + (3h)^2},$$
$$L_2(d, h) = \sqrt{d^2 + h^2} + 3h. \tag{A.11}$$

Furthermore, assuming the material depth is much larger than the distance between the transmitter and receiver, that is, $h \gg d$, the minimum and maximum path lengths can be approximated as,

$$\{L_2\}_{\min} \cong 2h,$$
$$\{L_2\}_{\max} \cong 4h. \tag{A.12}$$

Therefore, multipath II-A will approximately be in range $[2h\ 4h]$ as in multipath I.

Acknowledgment

References

[1] K. E. Thomenius, "Evolution of ultrasound beamformers," in *Proceedings of IEEE Ultrasonics Symposium*, pp. 1615–1622, November 1996.

[2] B. W. Drinkwater and P. D. Wilcox, "Ultrasonic arrays for non-destructive evaluation: a review," *NDT & E International*, vol. 39, no. 7, pp. 525–541, 2006.

[3] L. W. Schmerr and S.-J. Song, *Ultrasonic Nondestructive Evaluation Systems*, Springer, 2007.

[4] R. Lasser, M. Lasser, J. Kula, D. Ecich, and R. Westeric, "Remote, simple nondestructive testing of composite defects with an ultrasound camera: a Boeing study," in *Procceedings of Composites*, Las Vegas, Nev, USA, February 2010.

[5] C. Holmes, B. W. Drinkwater, and P. D. Wilcox, "Post-processing of the full matrix of ultrasonic transmit-receive array data for non-destructive evaluation," *NDT & E International*, vol. 38, no. 8, pp. 701–711, 2005.

[6] J. Zhang, B. W. Drinkwater, P. D. Wilcox, and A. J. Hunter, "Defect detection using ultrasonic arrays: the multi-mode total focusing method," *NDT & E International*, vol. 43, no. 2, pp. 123–133, 2010.

[7] P. Viswanath and D. Tse, *Fundamentals of Wireless Communications*, Cambridge University, 2005.

[8] V. Tarokh, Ed., *New Directions in Wireless Communications Research*, Springer, 2009.

[9] "Multipath Exploitation Radar (MER)," DARPA, Solicitation Number: DARPA-BAA-09-01.

[10] E.-G. Paek, J. Y. Choe, P. A. Bernhardt, and J. Horlick, "High-resolution over-the-horizon radar using time reversal," Tech. Rep. NRL/FR/5317-09-10,180, Naval Research Laboratory, December 2009, http://www.dtic.mil/cgi-bin/GetTRDoc?AD=ADA514533&Location=U2&doc=GetTRDoc.pdf.

[11] S. Kidera, T. Sakamoto, and T. Sato, "Experimental study of shadow region imaging algorithm with multiple scattered waves for UWB radars," *PIERS Online*, vol. 5, no. 4, pp. 393–396, 2009.

[12] P. Setlur, G. E. Smith, F. Ahmad, and M. Amin, "Target localization with a single-antenna monostatic radar via multipath exploitation," in *Proceedings of the SPIE Conference on Radar Sensor Technology XV*, Orlando, Fla, USA, April 2011.

[13] A. Derode, P. Roux, and M. Fink, "Robust acoustic time reversal with high-order multiple scattering," *Physical Review Letters*, vol. 75, no. 23, pp. 4206–4209, 1995.

[14] J. M. F. Moura and Y. Jin, "Detection by time reversal: single antenna," *IEEE Transactions on Signal Processing*, vol. 55, no. 1, pp. 187–201, 2007.

[15] J. Blitz and G. Simpson, *Ultrasonic Methods of Nondestructive Testing*, Chapman & Hall, 1996.

[16] J. Saniie and D. T. Nagle, "Pattern recognition in the ultrasonic imaging of reverberant multilayered structures," *IEEE Transactions on Ultrasonics, Ferroelectrics, and Frequency Control*, vol. 36, no. 1, pp. 80–92, 1989.

[17] J. D. Achenbach, L. Adler, D. K. Lewis, and H. McMaken, "Diffraction of ultrasonic waves by penny-shaped cracks in metals: theory and experiment," *Journal of Acoustical Society of America*, vol. 66, no. 6, pp. 1848–1856, 1979.

[18] R. Demirli, X. Rivenq, Y. D. Zhang, C. Ioana, and M. G. Amin, "MIMO array imaging for ultrasonic nondestructive testing," in *Nondestructive Characterization for Composite Materials, Aerospace Engineering, Civil Infrastructure, and Homeland Security*, vol. 7983 of *Proceedings of SPIE Conference*, San Diego, Calif, USA, March 2011.

[19] M. G. Amin and K. Sarabandi, "Special issue on remote sensing of building interior," *IEEE Transactions on GeoScience and Remote Sensing*, vol. 47, pp. 1267–1268, 2009.

[20] Y. D. Zhang and A. Hunt, "Image and localization of behind-the-wall targets using linear and distributed aperture," in *Through the Wall Radar Imaging*, chapter 4, CRC Press, 2010.

[21] Physical Acoustics Corporation products, http://www.pacndt.com/index.aspx?go=products.

[22] Olympus NDT contact transducers, http://www.olympus-ims.com/en/ultrasonic-transducers/contact-transducers/.

[23] M. Skolnik, *Radar Handbook*, McGraw-Hill, 3rd edition, 2007.